

Theoretical Studies on Electronic States of *Rh-C*₆₀. Possibility of a Room-temperature Organic Ferromagnet

S. Nakano ¹, Y. Kitagawa ^{1,*}, T. Kawakami ¹, M. Okumura ¹, H. Nagao ² and K. Yamaguchi ¹

¹ Department of Chemistry, Graduate School of Science, Osaka University, Toyonaka, Osaka 560-0043, Japan.

² Department of Computational Science, Faculty of Science, Kanazawa University, Kanazawa, Ishikawa 920-1192, Japan.

* Author to whom correspondence should be addressed; e-mail: kitagawa@chem.sci.osaka-u.ac.jp.

Received: 1 April 2004 / Accepted: 3 May 2004 / Published: 31 August 2004

Abstract: A possible mechanism for a ferromagnetic interaction in the rhombic (*Rh*) form of C₆₀ (*Rh-C*₆₀) is suggested on the basis of theoretical studies in relation to cage distortion of the C₆₀ unit in the polymerized 2D-plane. Band structure calculations on *Rh-C*₆₀ show that cage distortion leads to competition between diamagnetic and ferromagnetic states, which give rise to the possibility of thermally populating the ferromagnetic state.

Keywords: Ferromagnetic *Rh-C*₆₀, fullerene, tight binding band calculation.

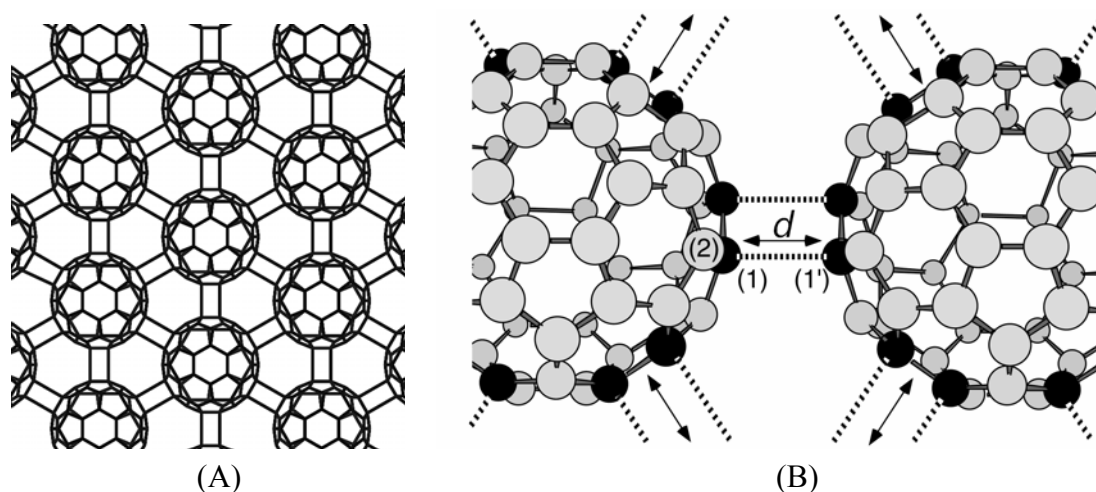
Introduction

The fullerene C₆₀ has attracted much interest since its discovery by Kroto *et al.* [1] because of its symmetric structure. After the discovery of a synthetic route to fullerenes by Krätschmer *et al.* many interesting physical properties have been reported [2]. It is well-known that C₆₀ is the most symmetric molecule, exhibiting icosahedral symmetry (*I*_h) with 120 symmetry operators. This symmetry leads to a highly degenerate set of molecular orbitals (MO), including five-fold degenerate HOMO (*H*_g) and three-fold degenerate LUMO (*T*_u). It has been reported that there are several types of lattice structures in solid states C₆₀ such as *f.c.c.* [3,4] and *b.c.c.*, as well as a two dimensionally (2D) polymerized rhombohedral lattice [5]. This rhombohedral phase (*Rh-C*₆₀) [Figure 1 (A)] was originally produced

by Iwasa *et al.* under high pressure and high temperature and a number of studies on its properties have been reported [6,7]. Recently, Makarova *et al.* reported weak ferromagnetism in *Rh-C*₆₀ [8] with a conspicuously high Curie temperature ($T_c \approx 500\text{K}$). Magnetic studies on a number of other molecule-based fullerene derivatives have exhibited substantially lower magnetic ordering temperatures e.g. tetrakis(dimethylamino)ethylene-fullerene (TDAE)-*C*₆₀ becomes ferromagnetic below 16.1K [9], whilst *La@C*₈₂ is paramagnetic [10] and antiferromagnetic ordering has been observed in $(\text{NH}_3)_3\text{K}_3\text{C}_{60}$ below 45 K [11,12]. In all these cases the magnetism is believed to originate from the magnetic moment on the charged fullerene after doping. Since *Rh-C*₆₀ is constructed only by carbon, there appears to be no doping mechanism, which leads us to a different mechanism from other fullerenes.

Interactions between *C*₆₀ units in 2D-*Rh-C*₆₀ may be classified into two types; inter-layer and intra-layer. The first type is weak and is almost the same as interactions observed in pristine *C*₆₀. The second one is considered to be a strong interaction between hexagon faces of neighbouring *C*₆₀ units, illustrated by gray and black circles, respectively in Figure 1 (B). Although many experimental and theoretical studies have been performed for this material, the electronic states have not still been elucidated. In this study, the electronic states of *Rh-C*₆₀ are examined using *ab initio* band structure calculations, focusing particularly on the effect of distortions of the *C*₆₀ cage in the polymerized 2D-plane, specifically: (i) the *sp*²-*sp*³ rehybridization, (ii) the band structure and the effect of distortion of *C*₆₀ cage with variation of distortion parameter *d* and (iii) the relative stability of low spin and high spin state of *Rh-C*₆₀ with variation of *d*.

Figure 1. The crystal structure of *Rh-C*₆₀. The cell parameters were obtained by Ref. 8. (A) 2D slab of *Rh-C*₆₀ on x-y plane; (B) Covalently bonding carbon (black circles) and the other carbons (gray circles); *d* is the distortion parameter. Only C* (black circles) were distorted.



Experimental background

The rhombohedral form of C_{60} was first reported by Iwasa *et al.* [5] who found that fullerene can be converted into two different structures by the application of high pressures and temperatures. Between 573 K and 673 K at 5 GPa, a *f.c.c.* structure was produced with lattice parameter $a = 13.6\text{\AA}$, whilst at higher temperatures (773 to 1073 K) at the same pressure, C_{60} was transformed into a rhombohedral structure with hexagonal lattice parameters of $a = 9.22\text{\AA}$, $c = 24.6\text{\AA}$ and space group *R-3m*. These two structures are metastable and revert to pristine C_{60} upon reheating up to 573 K at ambient pressure.

Subsequent studies by Makarova *et al.* have investigated the physical properties of *Rh-C*₆₀ which showed some dependence on the preparative conditions [8]. The stability limit of the C_{60} cage is 1073 – 1173 K at 6 GPa, above which there is a transition from *Rh-C*₆₀ to amorphous carbon. As a consequence, samples of ferromagnetic *Rh-C*₆₀ were synthesized close to the stability limit of the C_{60} cage; *Rh-C*₆₀ prepared at 923 K and 6 GPa exhibits semiconductor-like behavior, while materials synthesized at temperatures above the polymerisation limit showed some anisotropy of their electrical properties. Five out of six samples synthesized between 1025 K and 1050 K exhibited ferromagnetic behavior. This behavior was observed in 2D polymerized *Rh-C*₆₀ but not 1D orthorhombic C_{60} .

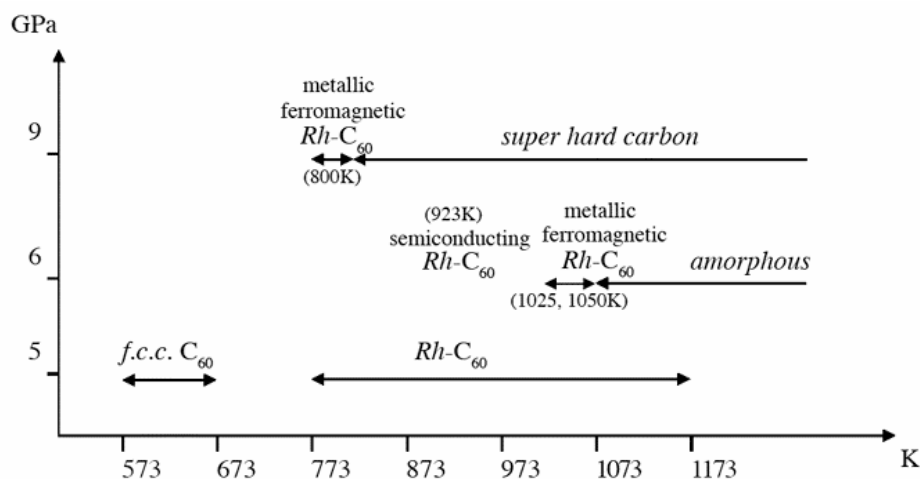
This ferromagnetic *Rh-C*₆₀ exhibits a pentagonal pinch $A_g(2)$ vibrational mode at 1407cm^{-1} in its Raman spectra. The mode frequencies of them correspond to those of normal *Rh-C*₆₀ and suggest only subtle structural differences between ferromagnetic *Rh-C*₆₀ and normal *Rh-C*₆₀. Indeed X-ray diffraction patterns of ferromagnetic *Rh-C*₆₀ indicates that its cell constants ($a = 9.204\text{\AA}$, $c = 24.61\text{\AA}$, with space group *R-3m*) are quite similar to those of normal *Rh-C*₆₀. The observed magnitude of magnetic susceptibility of ferromagnetic *Rh-C*₆₀ was 100 times larger than that for graphite and 10,000 times larger than that for pristine C_{60} . The spin concentration was $5 \times 10^{18}\text{cm}^{-3}$. The magnetic moment was estimated as $0.4\mu_B$, where μ_B is the Bohr magneton.

Makarova *et al.* [13] rationalised the experimental observations of the electronic properties of *Rh-C*₆₀ as follows: (i) anisotropic properties corresponding to in-plane and out-of-plane conductivity and (ii) metallic-like behavior due to in plane conductivity at high temperature which decreased with decreasing temperature. However, in relation to this metallic behaviour, the necessary sp^2 - sp^3 rehybridization mechanism required for the [2+2] cycloaddition between facial carbons of fullerenes, cannot be possible since the sp^2 - sp^3 rehybridization process supports the magnetic behaviour of *Rh-C*₆₀ rather than its metallic properties. The facial C atoms forming sp^3 hybrid orbitals will bear electron spins. However, as mentioned above, experimental results, conductivity mitigate against this mechanism since the ‘dangling bond’ associated with an sp^3 hybridised facial C indicates strong localization of the electron on pristine C_{60} , while the observed conductivity indicates itinerant behaviour.

Production of magnetic domains in *Rh-C*₆₀ was independently reported by another group [14]. Wood *et al.* synthesized polymerized *Rh-C*₆₀ in the region 700~1200 K under 9 GPa pressure. They indicated that *Rh-C*₆₀ synthesized at 800 K exhibited magnetism, while the C_{60} cage collapsed above

850 K in good agreement with previous observations. Therefore, near the stability limit of C_{60} cage, they also found the ferromagnetic fullerene. The summary of these experimental results can be expressed in the form of a phase diagram (Figure 2)

Figure 2. The summary of experimental results. Experimentally observed phases are listed.



Computational details

In this study, the LCAO tight binding approximation has been utilized with hybrid density functional theory, using the CRYSTAL98 program package. The computational method was Becke's 3 parameter functional combined with the non-local Lee-Yang-Parr correlation (B3LYP) and a 6-21G basis set of Gaussian-type orbitals. As the auxiliary basis set for fitting exchange and correlation potentials as well as the electron density, one *s*-type orbital, two *d*-type orbitals and one *f*-type orbital were applied. In the CRYSTAL98 program package, numerical accuracy was controlled mainly by five parameters (ITOL1-ITOL5) and the number of k points. $ITOL_x$ ($x=1-5$) control truncation criteria for two-electron integrals. Because low $ITOL_x$ values lead to inaccurate density matrix, we set $ITOL_{1-4} = 10$, $ITOL_5 = 18$. The space group and cell parameters were taken from experimental results (space group R-3m, $a=9.204\text{\AA}$, $c=24.61\text{\AA}$). The number of k-points in the irreducible Brillouin Zone (BZ) was 32 points. All C-C bonds within C_{60} were assumed to be 1.40\AA .

Several allotropes of carbon were examined using this approach, including graphite, diamond and *f.c.c.* C_{60} in order to verify the accuracy of this approach, with respect to band gap and structure. These data are available as Supplementary Information at the end of this paper. These calculations reproduce the semi-metal character of graphite, as well as a band gap in diamond (5.5 - 5.8 eV) in good agreement with experimental values (5.4 - 5.6 eV [15]). For *f.c.c.* C_{60} the calculated band gap was 2.0 eV (*c.f.* experimental value of 1.5 eV).

sp^2 - sp^3 rehybridization

In order to examine the possibility of sp^2 - sp^3 rehybridization, that is, production of dangling bonds on the C^* atom [labeled (1) and (1') in Figure 1 (B)], we have performed a comparative study of their bond population in comparison to sp^3 hybridised diamond (bond population = 0.319) and sp^2 -hybridised graphite (bond population = 0.440). Table 1 lists the bond populations on the $C^*(1)$ -C(2) and $C^*(1)$ - $C^*(1')$ bonds. On the basis of these results, $Rh-C_{60}$ is considered to have a sp^2 hybrid orbital. Despite the fullerene cage distortion, the bond population on $C^*(1)$ - $C^*(1')$ bond was not changed substantially. Since *f.c.c.* fullerene also exhibits an sp^2 hybrid orbital, the possibility of sp^2 - sp^3 rehybridization is unlikely and in agreement with the metallic character of $Rh-C_{60}$ reported by Makarova *et al.*

Table 1 Mulliken bond populations of several C-C bonds calculated by the B3LYP method.

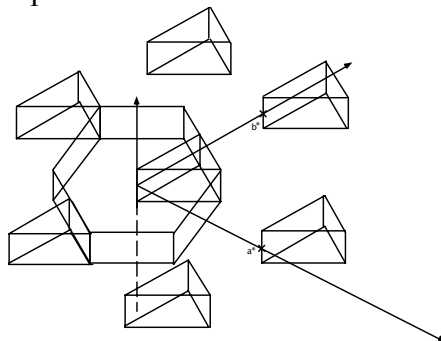
| Model | $C^*(1)$ -C(2) | $C^*(1)$ - $C^*(1')$ |
|----------------------|----------------|----------------------|
| C_{60} (R-3m) | 0.459 | 0.008 |
| C_{60} (Fm-3) | 0.427 | 0.005 |
| Graphite | 0.440 | |
| Diamond | 0.319 | |
| $Rh-C_{60}$ (d=8.3%) | 0.417 | 0.013 |

The band structure of $Rh-C_{60}$

Group theoretical prediction

Before the calculation of band structures, the splitting or degeneracy of energy band is predicted from a group theory examination. Figure 3 illustrates the B.Z. of $Rh-C_{60}$ crystal. The symmetry of this B.Z. is D_{3d} , which is a subgroup of I_h .

Figure 3. The reciprocal space around the first B.Z. The cross points (\times) denote reciprocal lattice points.



Under the empty lattice approximation, the Bloch function is expressed as

$$\psi_{\mathbf{k}n}(\mathbf{r}) = e^{i\mathbf{k}\cdot\mathbf{r}} u_{\mathbf{k}n}(\mathbf{r}) \tag{1a}$$

$$u_{\mathbf{k}n}(\mathbf{r}) = e^{i\mathbf{K}\cdot\mathbf{r}} \tag{1b}$$

for which the energy corresponding to this wavefunction is

$$E_{n\mathbf{k}}(\mathbf{k}) = \frac{\hbar^2}{2m} (\mathbf{k} + \mathbf{K})^2, \tag{2}$$

where \mathbf{k} and \mathbf{K} denote wave number and reciprocal lattice vectors respectively. When the behavior at Γ -point is in the question, \mathbf{k} set to be zero in eq.(2). Then the following eight functions (3a-h) which satisfy $E = E_0$ were constructed,

$$\psi_a = e^{i2\pi x/a}, \quad \psi_b = e^{-i2\pi x/a} \tag{3a),(3b}$$

$$\psi_c = e^{i2\pi(x/2+\sqrt{3}y/2)/a}, \quad \psi_d = e^{-i2\pi(x/2+\sqrt{3}y/2)/a} \tag{3c),(3d}$$

$$\psi_e = e^{i2\pi(-x/2+\sqrt{3}y/2)/a}, \quad \psi_f = e^{-i2\pi(-x/2+\sqrt{3}y/2)/a} \tag{3e),(3f}$$

$$\psi_g = e^{i2\pi z/a}, \quad \psi_h = e^{-i2\pi z/a} \tag{3g),(3h}$$

By operating the elements that belonged to the group of Γ in Table 2, the following reducible representation was obtained and it could be resolved as

$$\begin{matrix} E & 2C_3 & 3C_2 & i & 2S_6 & 3\sigma_d \\ 8 & 2 & 2 & 0 & 0 & 2 \end{matrix} \rightarrow 2\Gamma_1+\Gamma_3+\Gamma_4+\Gamma_5+\Gamma_6.$$

Table 2. Character table for G-point of rhombohedral lattice

| Γ | E | $2C_3$ | $3C_2$ | i | $2S_6$ | $3\sigma_d$ |
|------------|---|--------|--------|----|--------|-------------|
| Γ_1 | 1 | 1 | 1 | 1 | 1 | 1 |
| Γ_2 | 1 | 1 | -1 | 1 | 1 | -1 |
| Γ_3 | 2 | -1 | 0 | 2 | -1 | 0 |
| Γ_4 | 1 | 1 | 1 | -1 | -1 | -1 |
| Γ_5 | 1 | 1 | -1 | -1 | -1 | 1 |
| Γ_6 | 2 | -1 | 0 | -2 | 1 | 0 |

Using the projection operator method[18], the following linear combination of Bloch functions were obtained.

$$\psi(\Gamma_1)_i \propto \psi_a + \psi_b + \psi_c + \psi_d + \psi_e + \psi_f \tag{4a}$$

$$\psi(\Gamma_1)_j \propto \psi_g + \psi_h \tag{4b}$$

$$\psi(\Gamma_3)_i \propto \psi_a + \psi_b - \psi_d - \psi_e \tag{4c}$$

$$\psi(\Gamma_3)_j \propto \psi_a + \psi_b - \psi_c - \psi_f \tag{4d}$$

$$\psi(\Gamma_3)_k \propto -\psi_b + \psi_c + \psi_d - \psi_f \tag{4e}$$

⋮

Using the following relations, $\cos x \approx 1+x$ and $\sin x \approx x$, these wavefunctions can be rewritten as

$$\psi(\Gamma_1)_i \approx x^2 + y^2 = 1, \quad \psi(\Gamma_1)_j \approx z^2 \quad (5a),(5b)$$

$$\psi(\Gamma_3)_i \approx x^2 - y^2, \quad \psi(\Gamma_3)_j \approx xy \quad (5c),(5d)$$

$$\psi(\Gamma_4) \approx 0, \quad \psi(\Gamma_5) \approx z \quad (5e),(5f)$$

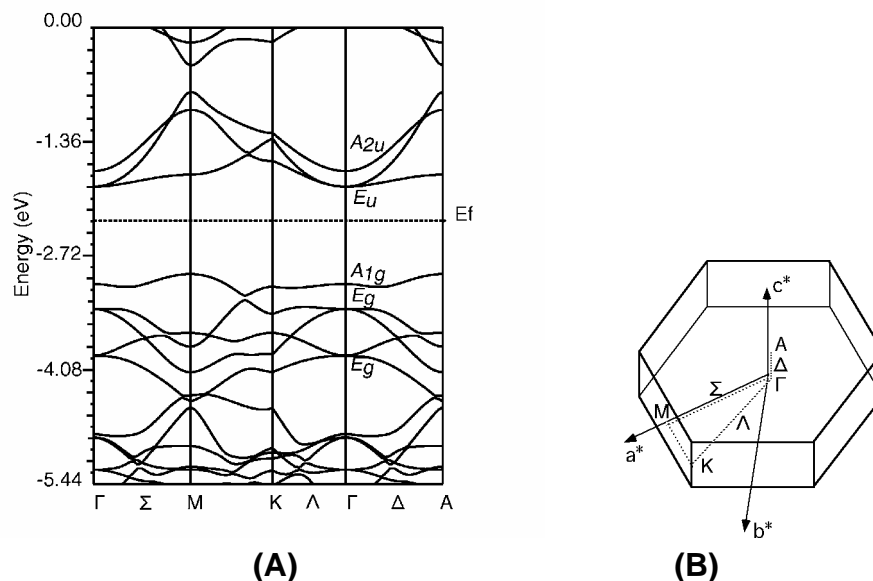
$$\psi(\Gamma_6)_i \approx x, \quad \psi(\Gamma_6)_j \approx y \quad (5g),(5h)$$

According to the character table of I_h which pristine C_{60} belongs to, the three-fold degenerate LUMOs split into a singly-degenerate $\psi(\Gamma_5)$ and two-fold degenerate $\psi(\Gamma_6)$, whilst the five-fold degenerate HOMOs split into a singly-degenerate $\psi(\Gamma_4)$ and two-fold degenerate $\psi(\Gamma_1)$ and $\psi(\Gamma_3)$. These predictions were confirmed by the following band calculations.

Rh-C₆₀ without distortion of C₆₀ cage

Figure 4 illustrates the band structure of normal *Rh-C₆₀* i.e. without cage distortion. Each special points were defined as Γ (0, 0, 0), M (1/2, 0, 0), K (1/3, 1/3, 0), A (0, 0, 1/2) as illustrated in the B.Z. Valence and conduction bands were separated by the broken line (E_f = Fermi level).

Figure 4 (A) The band structure of normal *Rh-C₆₀* ($d = 0\%$); (B) The first B.Z. with special points and line. The detail information is given in the text.



The two lowest conduction bands (LCB) were essentially two-fold degenerate at the Γ point. According to the IR-active modes[6], we confirmed that LCB showed the interaction of C^*-C^* bond between C_{60} units. Conversely, the highest valence band (HVB) was non-degenerate. This split of HVB from the five-fold degenerated H_g came from anisotropic structure of the rhombohedral phase. Namely, LCB and HVB corresponded to (x,y) and z^2 symmetry respectively. Therefore if the LCB are

stabilized, they can get closer to the HVB without repulsion because they are mutually orthogonal. The calculated band gap was 1.23 eV, reproducing the semi-conducting nature of normal *Rh-C₆₀*.

Rh-C₆₀ with distortion of *C₆₀* cage

Since the LCB expresses the inter-fullerene interaction, it is expected that these LCB will be stabilized when the distance of inter-fullerene become shorter. A distortion parameter *d* was defined as

$$d = (D_0 - D) \times 100 / D_0 \quad (6)$$

where *D* and *D₀* denote the inter-fullerene distance with and without distortion, respectively (i.e. *D₀* = 2.408 Å, *D* < 2.408 Å). By varying the parameter *d*, the LCB were stabilized as shown in Figure 5. Table 3 shows the variation in the Fermi energy (*E_F*) and band gap (*E_g*) as a function of this distortion parameter.

Figure 5. The band structures of *Rh-C₆₀* with distortion (A) *d* = 2.08% (B) *d* = 4.15% (C) *d* = 8.30% (D) The Fermi-Dirac distribution under the distortion *d* = 8.30%. The metallic character was expected judging from (C) and (D).

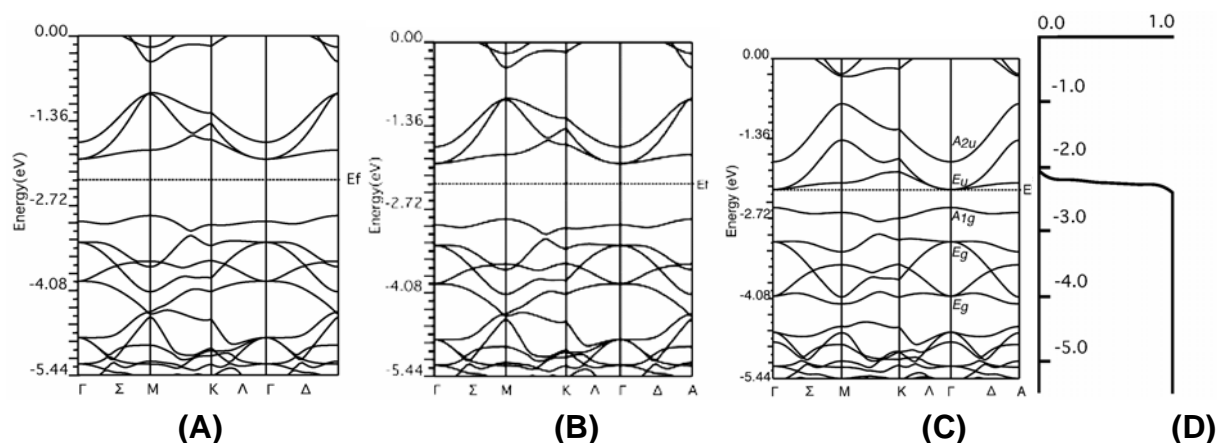
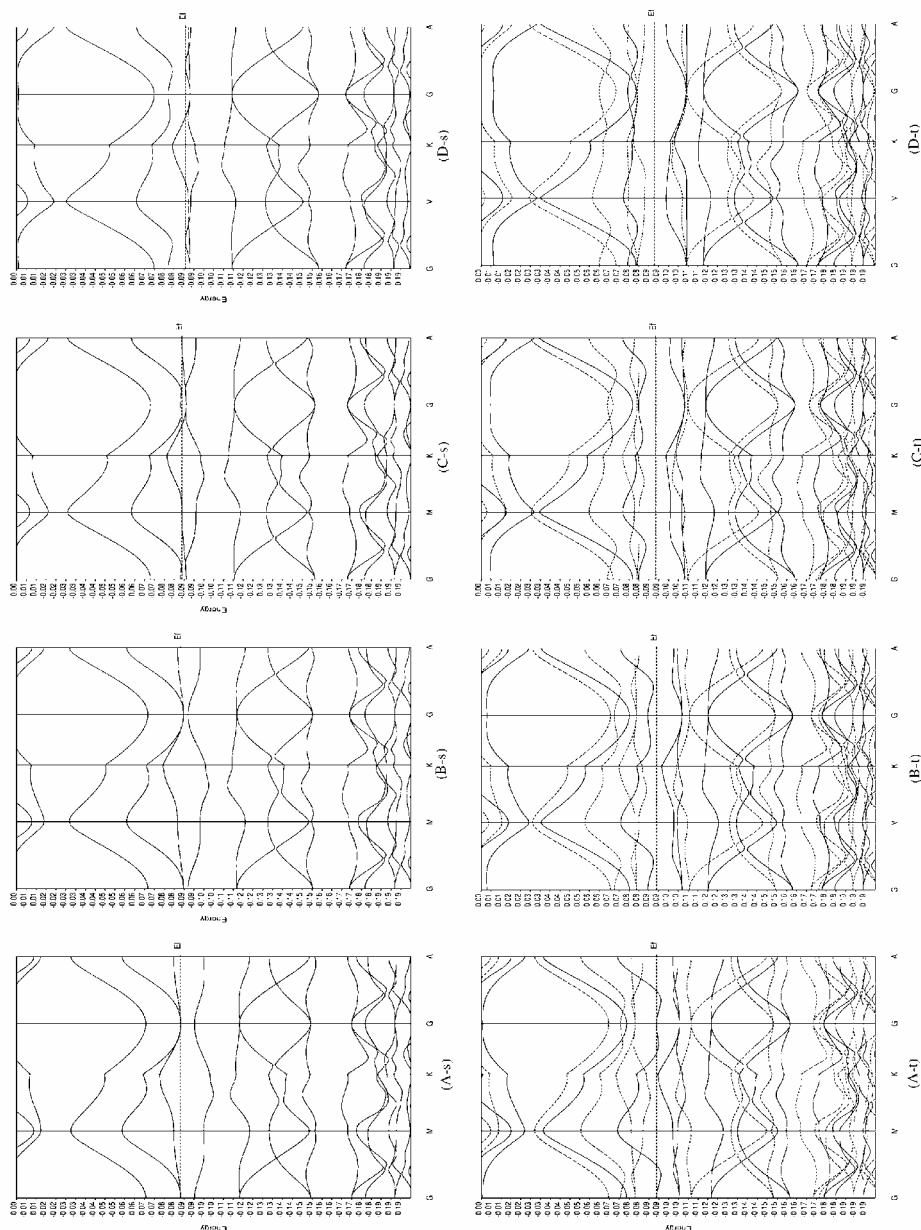


Table 3. Calculated band gaps* (*E_g*) and Fermi level* (*E_F*) with variation of distortion parameter *d*

| <i>d</i> | <i>E_g</i> | <i>E_F</i> |
|----------|----------------------|----------------------|
| 0.00 | 1.23 | -2.30 |
| 2.08 | 1.00 | -2.30 |
| 4.15 | 0.75 | -2.30 |
| 8.30 | 0.31 | -2.24 |

* in eV

Figure 6 The upper four band structures (X-s: X=A, B, C, D) correspond singlet *Rh-C*₆₀ with distortion (A) $d = 9.14$, (B) $d = 9.97$, (C) $d = 10.80$, (D) $d = 11.63$, respectively. Similarly, the lower four band structures (X-t: X=A, B, C, D) correspond triplet *Rh-C*₆₀ with distortion (A) $d = 9.14$, (B) $d = 9.97$, (C) $d = 10.80$, (D) $d = 11.63$, respectively. Atomic unit was used for energy. The band structure (D-s) includes flat band.



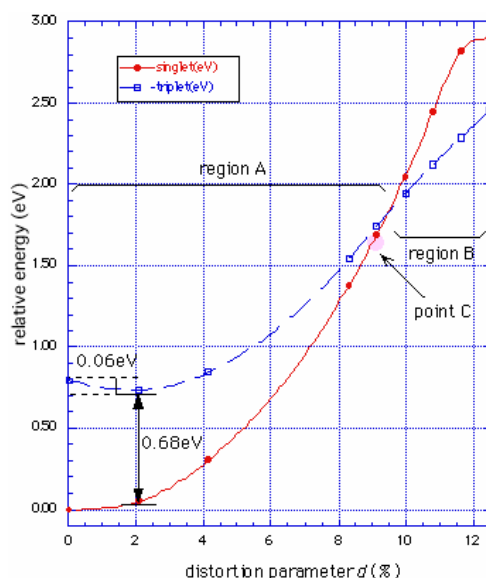
An analysis of these results indicates that the greater distortion of the *C*₆₀ cage leads to a decrease in the band gap, E_g . Considering the Fermi-Dirac distribution at room temperature ($T=300\text{K}$), *Rh-C*₆₀ is expected to become metallic in agreement with the experimentally observed semiconductor-metal phase transition [8]. It is noteworthy that the dispersion of the HVB is considerably small, that is, a

flat band was observed. The LCB and this HVB became closer and closer as d increased. Of particular note is the case when $d = 11.6\%$. At this point one of the LCB and the HVB form a two-fold degenerate half-filled flat bands around the Fermi level as shown in Figure 6.

According to the Mielke-Tasaki theorem [17], this band structure satisfies the necessary condition for flat band ferromagnetism. Thus if on-site Coulomb repulsion U on fullerene is not zero, the ferromagnetic electronic state may be one of the possible ground states. In order to elucidate the possibility of ferromagnetic ground state, an examination of the relative stability of this ferromagnetic state is necessary.

Figure 7 shows the relative energies of the singlet (diamagnetic) and triplet (ferromagnetic) states per unit cell. From Figure 7, we observed four distinct regions as follows: (1) For small d ($0 \leq d \leq 9.5\%$, labelled A in Figure 7), the singlet state was more stable than triplet state. Since normal $Rh-C_{60}$ was considered to be semi-conducting, this is consistent with experimental results. (2) An energy minimum for the triplet state at $d = 2\%$. The energy of this triplet is stabilized by 0.06 eV compared to the undistorted structure ($d=0\%$). However the triplet is still substantially higher in energy than the singlet at this point (0.68 eV) and so a contribution of the triplet state to the magnetic properties would appear negligible in region A (Figure 7). (3) In region B ($d > 9.5\%$) the triplet state is now more stable than the singlet. Thus in this region, a ferromagnetic $Rh-C_{60}$ electronic state is expected arising from flat band ferromagnetism. It is, however, considered that this ferromagnetic phase is different from the experimental ferromagnetic phase since three calculations reveal a finite band gap (semi-conductor) behaviour whereas the experimental studies indicate metallic behavior. (4) At the point of $d \approx 9.5\%$, crossing of the singlet and triplet states occurs.

Figure 7. S-T gap of $Rh-C_{60}$ with variation of C_{60} cage distortion. The information of region and point are in the text.



Around the boundary between regions A and B, the triplet and singlet states are competitive. From the band structure of the singlet state at this boundary, a metallic state is predicted as the ground state, consistent with the experimental study. One possibility to explain the mechanism of ferromagnetism in *Rh-C₆₀* could be proposed. (1) The experimental ferromagnetic *Rh-C₆₀* phase occurs around point C, which is found at a distortion d just below the intersection of the singlet and triplet energies (Figure 7) which leads to metallic behaviour observed in the experimental ferromagnetic *Rh-C₆₀*. (2) The singlet-triplet gap at the point C is so small that some thermal population of the triplet state may occur. This thermally induced triplet *Rh-C₆₀* can be considered as an experimentally observed magnetic domain. The population in the excited state at the various temperatures were estimated by the Boltzmann distribution

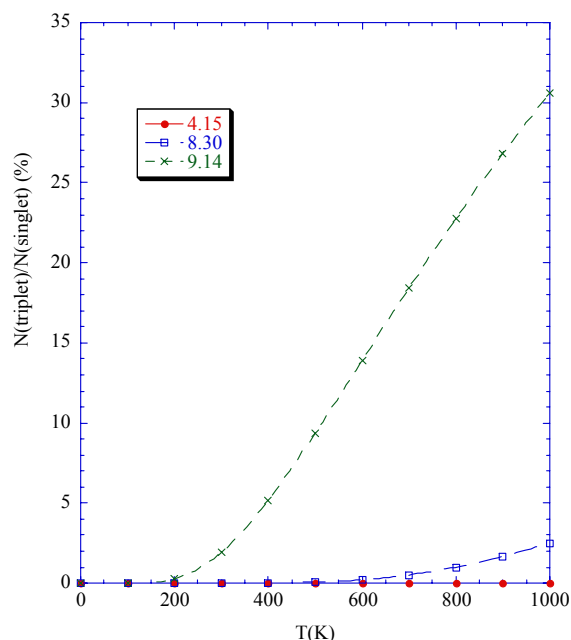
$$\frac{N(\text{triplet})}{N(\text{singlet})} = e^{-\frac{(E_{\text{triplet}} - E_{\text{singlet}})}{kT}}, \quad (8)$$

as illustrated in Figure 8. The percentage of triplet is expected to be 2% at 300 K with $d = 9.1\%$. Using this percentage of triplet, the spin concentration value (n) be estimated as follows:

$$n = \frac{N(\text{triplet})}{N(\text{singlet}) + N(\text{triplet})} \left(\frac{S}{V} \right), \quad (9)$$

where V and S denote the volume of primitive cell ($=601.8 \times 10^{-24} \text{cm}^3$) and spin magnitude ($=2$), respectively. The estimated value is $6.6 \times 10^{19} \text{cm}^{-3}$, is comparable with the experimental value ($5 \times 10^{18} \text{cm}^{-3}$) despite the simplicity of this approximation.

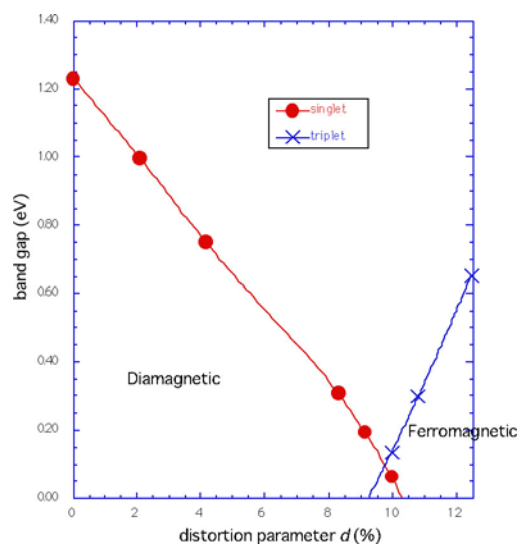
Figure 8. The proportion of triplet and singlet under the temperature 0~1000K. Each line is obtained from distorted structure $d = 4.15, 8.30, 9.14\%$, respectively.



Phase diagram

The investigation of the relationship among superconductivity, diamagnetic and ferromagnetic phases seemed to be attractive work. The phase diagram of $Rh-C_{60}$ with band gap (E_g) against d was illustrated in Figure 9. As the parameter d increases, diamagnetic and ferromagnetic phases disappeared and appeared, respectively. For superconducting materials, the existence of a singlet magnetic phase (singlet superconducting or spin density wave etc.) is expected between diamagnetic and ferromagnetic phases. However, in case of $Rh-C_{60}$, this singlet magnetic phase was not observed experimentally[8]. It is considered that the occurrence of the ferromagnetic phase prevents the appearance of a singlet magnetic phase because of the relative stability of ferromagnetic phase. Conversely the triplet superconductivity might be realized in the $Rh-C_{60}$ system.

Figure 9. The band gap of $Rh-C_{60}$ with increase of distortion parameter d . In case of $d = 0\sim 9.5\%$, diamagnetic phase was obtained, while $d > 9.5\%$, ferromagnetic phase was obtained.



Conclusions

In this paper, one possible mechanism to account for ferromagnetic $Rh-C_{60}$ was suggested on the basis of theoretical studies. Calculated band structures indicate the presence of a semiconducting-metallic phase transition with increase in the distortion parameter d . As d increases, the ferromagnetic state becomes stabilized in comparison with singlet state and finally becomes the ground state. This mechanism was considered to be associated with flat band ferromagnetism. However, the triplet state is expected to show semiconductor nature contrary to the experimental metallic character, whilst singlet state shows metallic results. Near the crossing of singlet and triplet states, the singlet-triplet gap is sufficiently small for some thermal population of the ferromagnetic state. This ratio was estimated

as at most 2% at 300K by Boltzmann distribution, yielding a spin concentration of $6.6 \times 10^{19} \text{cm}^{-3}$, in agreement with the experimental one. In conclusion, the cage distortion of C_{60} in polymerized 2D-plane $Rh\text{-C}_{60}$ leads to competition between diamagnetic and ferromagnetic states, with the ferromagnetic state populated by thermal excitation. Recently, several experimental and theoretical studies on $Rh\text{-C}_{60}$ polymers and related carbon systems have been reported [19-27]. Some of them support previous results by Makarova *et al.* The present results provide one possible explanation of these results. Further experimental and theoretical studies are necessary towards achieving the goal of a room-temperature organic magnet.

Acknowledgments

This work has been supported by a Grant-in-Aid for Scientific Research on Priority Areas (Nos. 16750049, 14204061 and 15750120) from The Ministry of Education, Culture, Sports, Science and Technology, Japan.

Supplementary Information

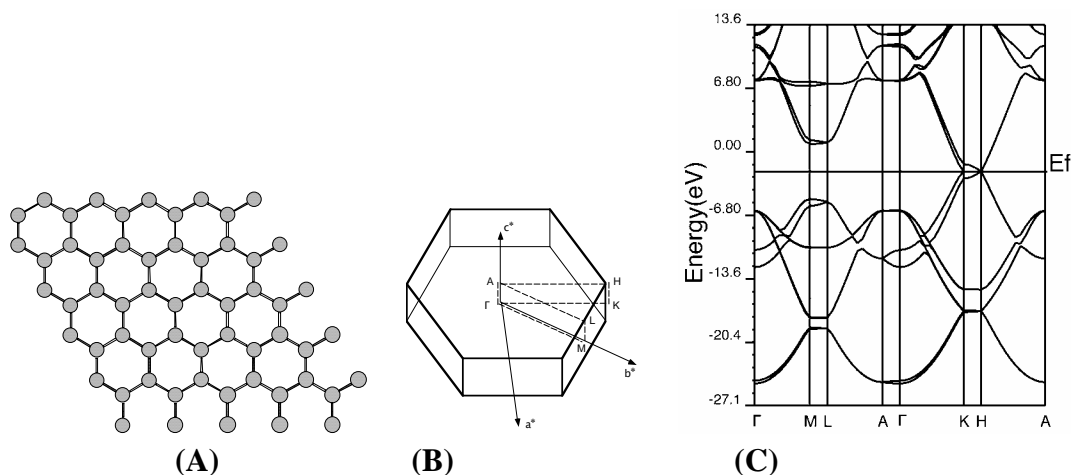
The verification of hybrid DFT band calculation

Before the calculation of $Rh\text{-C}_{60}$, several allotropes of carbon were examined by using the hybrid DFT band calculations. The calculated models were 2D-graphite, 3D-diamond, and *f.c.c.* (3D) fullerene. There are two purposes of these calculations. The first one is examination and verification of hybrid DFT band calculation from the view points of accuracy of band gap and shape of band structure. The second one is to obtain Mulliken bond population of sp^2 (graphite) and sp^3 (diamond) bond. This population expresses charge density on bond. Hence this value is dependance on its bond nature such as sp^2 and sp^3 , it is a useful index to investigate the bond nature. Calculations were performed under the following conditions; ITOL1 - 4 = 10, ITOL5 = 15, the energy convergence was 10^{-7} , the distance between carbons were set to be 1.40\AA . The calculation method was B3LYP, and basis set was 6-21G.

Graphite

Figures S1 (A) and (B) show the calculated models and the Brillouin Zones (B.Z.). Cell parameters was set to be $(a, b, c, \alpha, \beta, \gamma) = (2.43, 2.43, 6.70, 90, 90, 120)$ in $P63mc$ symmetry. Each special point in B.Z. denotes $\Gamma=(0, 0, 0)$, $M=(0, 1/2, 0)$, $L=(0, 1/2, 1/2)$, $A=(0, 0, 1/2)$, $K=(-1/4, 1/2, 0)$, $H=(-1/4, 1/2, 1/3)$. The number of k-points in irreducible B.Z. was 50. The calculated band structure, which was illustrated in Figure 3 (C), shows the semi-metal character, *i.e.* (i) overlap of conduction band and valence band, (ii) linear dispersion around the Fermi level was not quadratic dispersion. The calculated bond population was 0.440 as shown in Table 1 (see main text).

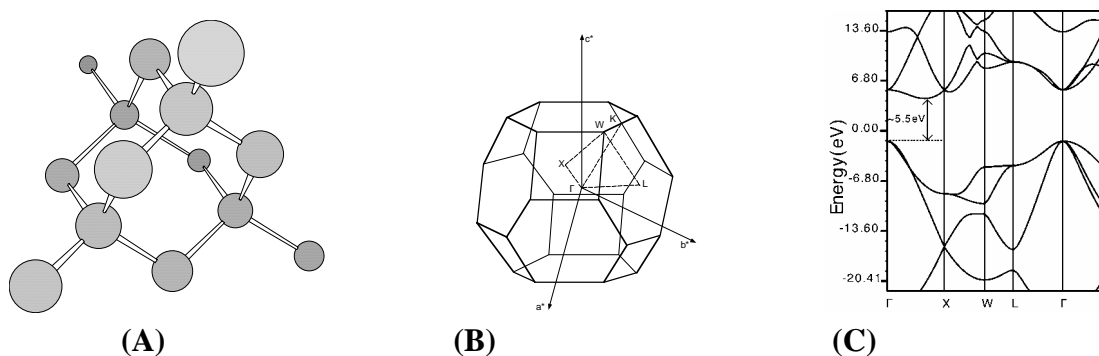
Figure S1. (A) The calculated model of graphite. (B) The calculated B.Z. (C) The obtained band structure. The detail information is given in the text.



Diamond

Figures S2 (A) and (B) show the model structure of diamond and its B.Z.. The R_{c-c} distance was set to be (a) 1.4Å and (b) 1.55Å [15]. The cell parameter was $(a, b, c, \alpha, \beta, \gamma) = (3.25, 3.25, 3.25, 90, 90, 90)$ in $Fd3m$ symmetry. FigureS2 (C) illustrates [15] the calculated band structure. Each special point denotes $\Gamma=(0, 0, 0)$, $X=(1/2, 0, 1/2)$, $W=(1/2, 1/4, 1/4)$, $L=(1/2, 1/2, 1/2)$, $K=(1/4, 1/4, 1/2)$. It successfully expresses the nature of indirect band gap between Γ -point and $3/4$ point of Γ -X path. Obtained band gaps were 5.5eV and 5.8eV with the structure (a) and (b), respectively. They are in good agreement with experimental values (5.4 - 5.6eV) [15]. On the other hand, BLYP, which is a pure DFT method, obviously underestimated the band gap as 4eV. The estimated bond population of diamond was 0.319. From these results, it is considered that B3LYP is an appropriate method for both sp^3 -diamond and sp^2 -graphite.

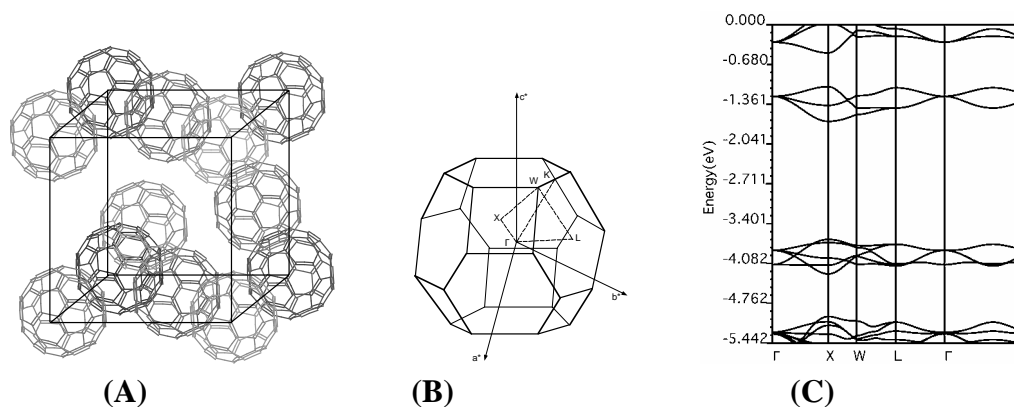
Figure S2 (A) The calculated model of diamond; (B) The calculated B.Z; (C) The obtained band structure. The detail information is given in the text.



f.c.c. fullerene

Figures S3 (A) and (B) show the *f.c.c.* fullerene and its B.Z. The cell parameters were $(a, b, c, \alpha, \beta, \gamma) = (14.0, 14.0, 14.0, 90, 90, 90)$ in *Fm-3* symmetry. The shape of B.Z. and the coordinates of special points were same as those of diamond. The calculated band gap was 2.0eV. Comparing with experimental value (1.5eV), B3LYP expresses semi-conducting nature of *f.c.c.* fullerene well. All these examinations support the justification of B3LYP band calculation for the carbon allotropes. The pure DFT (BLYP) underestimates their band gaps as usually expected from other cases.

Figure S3. (A) The calculated model of *f.c.c.* fullerene (B) The calculated B.Z. (C) The obtained band structure. The detail information is given in the text.



References and Notes

1. Kroto, H.W.; Heath, J.R.; O'Brien, S.C.; Curl, R.F.; Smalley, R.E. *Nature*, **1985**, *318*, 162.
2. Krätschmer, W.; Lamb, L.D.; Fostiropoulos, K.; Huffman, D.R. *Nature*, **1990**, *347*, 354.
3. Saito, S.; Oshiyama, A. *Phys. Rev. Lett.* **1991**, *66*, 2367.
4. Haddon, R. C. *Acc. Chem. Res.* **1992**, *25*, 127.
5. Iwasa, Y.; Arima, T.; Fleming, R.M.; Siegrist, T.; Zou, O.; Haddon, R.C.; Rothberg, L.J.; Lyons, K.B.; Carter Jr., H.L.; Hebard, A.F.; Tycko, R.; Dabbagh, G.; Krajewski, J.J.; Thomas, G.A.; Yagi, T. *Science* **1994**, *264*, 1570.
6. Long, V.C.; Musfeldt, J.L.; Kamarás, K.; Adams, G.B.; Page, J.B.; Iwasa, Y.; Mayo, W.E. *Phys Rev.* **2001**, *B61*, 13191.
7. Davydov, V.A.; Kashevarova, L.S.; Rakhmanina, A.V.; Senyavin, V.M.; Céolin, R.; Szwarc, H.; Allouchi, H.; Agafonov, V.; *Phys Rev.* **2000**, *B61*, 11936.
8. Makarova, T.M.; Sundqvist, B.; Höhne, R.; Esquinazi, P.; Kopelevich, Y.; Scharff, P.; Davydov, V.A.; Kashevarova, L.S.; Rakhmanina, A.V. *Nature* **2001**, *413*, 716.
9. Allemand, P.-M.; Khemani, K.C.; Koch, A.; Wudl, F.; Holczer, K.; Donovan, S.; Grüner, G.; Thompson, J.D. *Science* **1991**, *253*, 301.

10. Johnson, R. D.; Vries M. S; Salem, J.; Bethune, D. S; Yannoni, C. S. *Nature*, **1992**, *355*, 239.
11. Tou, H.; Maniwa, Y.; Iwasa, Y.; Shimoda, H.; Mitani, T. *Phys. Rev.* **2000**, *B62*, R775.
12. Kitano, H.; Matsuo, R.; Miwa, K.; Maeda, A.; Takenobu, T.; Iwasa, Y.; Mitani, T. *Phys. Rev. Lett.* **2002**, *88*, 096401.
13. Makarova, T.M.; Sundqvist, B.; Scharff, P.; Gaevski, M.E.; Olsson, E.; Davydov, V.A.; Rakhmanina, A.V.; Kashevarova, L.S. *Carbon* **2001**, *39*, 2203.
14. Wood, R.A.; Lewis, M.H.; Lees, M.R.; Bennington, S.M.; Cain, M.G.; Kitamura, N. *J. Phys. Condens. Matter*, **2002**, *14*, L385.
15. It was written in many textbooks, for example: Kittel, C. *Introduction to Solid State Physics*; John Wiley & Sons, Inc.: New York, **1986**.
16. Erwin, S.C. In *Buckminsterfullerenes*; Billups, W.E.; Ciufolini, M.A.; Eds.; VCH: New York, **1993**; p. 217.
17. Mielke, A.; Tasaki, H.; *Commun. Math. Phys.* **1993**, *158*, 341.
18. For instance, $\psi(\Gamma_3)_i$ was obtained as follows;

$$\psi(\Gamma_3)_i = \frac{l}{h} \{ (2)E\psi_a + (-1)C_3\psi_a + (-1)C'_3\psi_a + (0)C_2\psi_a + (0)C'_2\psi_a + (0)C''_2\psi_a + 2i\psi_a + (-1)S_6\psi_a + (-1)S'_6\psi_a + (0)\sigma_d\psi_a + (0)\sigma'_d\psi_a + (0)\sigma''_d\psi_a + \dots \}$$
 ,
 where l and h denote the dimension and order of symmetry on consideration.
19. Han, K.-H.; Spemann, D.; Höhne, R.; Setzet, A.; Makarova, T.; Esquinazi, P.; Butz, T. *Carbon* **2003**, *41*, 785.
20. Andriotis, A. N.; Menon, M.; Sheetz, R. M.; Chernozatonskii, L. *Phys. Rev. Lett.* **2003**, *90*, 026801.
21. Ribas-Ariño, J.; Novoa, J. J. *J. Phys. Chem. Solids*. **2004**, *65*, 787.
22. Okada, S.; Oshiyama, A. *Phys. Rev.* **2003**, *B68*, 23542.
23. Chi, D. H.; Iwasa, Y.; Takano, T.; Watanuki, T., Ohishi, Y.; Yamanaka, S. *Phys. Rev.* **2003**, *B68*, 153402.
24. Korobov, M. V.; Senyavin V. M; Bogachev, A. G.; Stukalin, E. B.; Davidov, V. A.; Kashevarona, L. S.; Rakhmanina, A. V.; Agafonov, V.; Szwarc, A. *Chem. Phys. Lett.* **2003**, *381*, 410.
25. Makarova, T. L.; Han, K.-H.; Esquinazi, P.; da Silva R. R.; Kopelevich, Y.; Zakharova, I. B.; Sundqvist, B. *Carbon*, **2003**, *41*, 1575.
26. Owens, F. J.; Iqhal, Z.; Belova, L.; Rao, K. V. *Phys. Rev.* **2004**, *B69*, 033403.
27. Nakano, S., Kitagawa, Y.; Kawakami, T.; Yamaguchi, T. *Synthetic Metals*, **2003**, *135-136*, 779.

Samples Availability: Available from the authors.